Princeton Plasma Physics Laboratory

PPPL-4198

PPPL-4198

# Characterization of Small, Type V ELMs in the National Spherical Torus Experiment

R. Maingi, M.G. Bell, E.D. Fredrickson, K.C. Lee, R.J. Maqueda,
P. Snyder, K. Tritz, S.J. Zweben, R.E. Bell, T.M. Biewer, C.E. Bush, J. Boedo,
N.H. Brooks, L. Delgado-Aparicio, C.W. Domier, D.A. Gates, D.W. Johnson,
R. Kaita, S.M. Kaye, H.W. Kugel, B.P. LeBlanc, N.C. Luhmann, Jr., J.E. Menard,
D. Mueller, H. Park, R. Raman, A.L. Roquemore, S.A. Sabbagh,
V.A. Soukhanovskii, T. Stevenson, and D. Stutman

December 2006

PPPL
PRINCETON PLASMA
PHYSICS LABORATORY

Prepared for the U.S. Department of Energy under Contract DE-AC02-76CH03073.

# Princeton Plasma Physics Laboratory
# Report Disclaimers

## Full Legal Disclaimer



## Trademark Disclaimer



# PPPL Report Availability

## Princeton Plasma Physics Laboratory:

http://www.pppl.gov/pub_report/

## Office of Scientific and Technical Information (OSTI):

http://www.osti.gov/bridge

## U.S. Department of Energy:

U.S. Department of Energy
Office of Scientific and Technical Information
P.O. Box 62
Oak Ridge, TN 37831-0062
Telephone: (865) 576-8401
Fax: (865) 576-5728
E-mail: reports@adonis.osti.gov

# Characterization of Small, Type V ELMs in the National Spherical Torus Experiment

R. Maingi 1), M.G. Bell 2), E.D. Fredrickson 2), K.C. Lee 3), R.J. Maqueda 4), P. Snyder 5), K. Tritz 6), S.J. Zweben 2), R.E. Bell 2), T.M. Biewer 1), C.E. Bush 1), J. Boedo 7), N.H. Brooks 5), L. Delgado-Aparicio 6), C.W. Domier 3), D.A. Gates 2), D.W. Johnson 2), R. Kaita 2), S.M. Kaye 2), H.W. Kugel 2), B.P. LeBlanc 2), N.C. Luhmann, Jr. 3), J.E. Menard 2), D. Mueller 2), H. Park 2), R. Raman 8), A. L. Roquemore 2), S.A. Sabbagh 9), V.A. Soukhanovskii 10), T. Stevenson 2), D. Stutman 5)

1) Oak Ridge National Laboratory
2) Princeton Plasma Physics Laboratory
3) Univ. California - Davis
4) Nova Photonics
5) General Atomics
6) Johns Hopkins University
7) Univ. California - San Diego
8) Univ. Washington
9) Columbia University
10) Lawrence Livermore National Laboratory

**Abstract**

There has been a substantial international research effort in the fusion community to identify tokamak operating regimes with either small or no periodic bursts of particles and power from the edge plasma, known as edge localized modes (ELMs). While several candidate regimes have been presented in the literature, very little has been published on the characteristics of the small ELMs themselves. One such small ELM regime, also known as the Type V ELM regime, was recently identified in the National Spherical Torus Experiment [M. Ono, S.M. Kaye, Y.-K.M. Peng, et. al., *Nucl. Fusion* **40**, 557 (2000)]. In this paper, the spatial and temporal structure of the Type V ELMs is presented, as measured by several different diagnostics. The composite picture of the

Type V ELM is of an instability with one or two filaments which rotate toroidally at ~ 5-10 km/sec, in the direction opposite to the plasma current and neutral beam injection. The toroidal extent of Type V ELMs is typically ~5m, whereas the cross-field (radial) extent is typically ~ 10 cm (3 cm), yielding a portrait of an electromagnetic, ribbon-like perturbation aligned with the total magnetic field. The filaments comprising the Type V ELM appear to be destabilized near the top of the H-mode pedestal and drift radially outward as they rotate toroidally. After the filaments come in contact with the open field lines, the divertor plasma perturbations are qualitatively similar to other ELM Types, albeit with only one or two filaments in the Type V ELM vs. more filaments for Type I or Type III ELMs. Preliminary stability calculations eliminate pressure driven modes as the underlying instability for Type V ELMs, but more work is required to determine if current driven modes are responsible for destabilization.

## I. Introduction

Performance projections for the International Thermonuclear Experimental Reactor (ITER) have highlighted the correlation between performance of the burning plasma core and the plasma temperature at the top of the H-mode pedestal. Studies examining many devices have shown[1, 2] that the highest pedestal temperature occurs at low pedestal collisionality, a region that is typically accompanied by large edge-localized modes (ELMs). Large or Type I ELMs result in a periodic exhaust of a substantial portion of the plasma stored energy to the plasma-facing components (PFCs). Localized melting of the PFCs would occur in ITER if the ELM energy deposition were to exceed the PFC heat handling capability, which would effectively impose a limit on the PFC lifetime[3].

Accordingly the quest for high confinement regimes with no or small ELMs has received high priority in the fusion research community. Several promising regimes have been identified which maintain the H-mode transport barrier: small, Type II ELMs from shaping[4-6] or high density operation[7, 8]; grassy ELMs[9]; the Enhanced $D_\alpha$ H-mode[10] and High Recycling Steady H-mode[11]; the Quiescent H-mode[12]; the small, Type V ELMs[13]; and the suppression of large ELMs with externally imposed edge resonant magnetic perturbations[14]. Advances in the understanding of the structure[15-23] of the ELMs and modeling of the underlying magnetohydrodynamic (MHD) instabilities[24-31] have accompanied the progress in identification of small ELM regimes.

ELM control research is an important part of the program in the National Spherical Torus Experiment (NSTX)[32, 33], owing partly to the importance for ITER described above and partly to the needs of long pulse operation. Spherical tori such as NSTX have limited space for an ohmic transformer, leading to lower volt-second capabilities than higher aspect ratio tokamaks. Large ELMs can penetrate substantially[34] into the core of NSTX, causing an increase in plasma resistivity, an increase in the ohmic flux consumption rate, and a decrease in the pulse length.

In this paper we discuss, for the first time, the spatial and temporal structure of small ELMs as interpreted through diagnostic signatures in NSTX. The remainder of this paper is organized as follows. In section II, a comparison of flux consumption with small and large ELMs is presented. In section III, the characteristics of the small ELMs as measured by several different diagnostics is presented. The results of preliminary stability

calculations and implications of the diagnostic observations to certain aspects of stability theory are discussed in section IV, followed by conclusions in section V.

## II. Flux consumption and pulse length with small ELMs

One of the by-products of a small aspect ratio tokamak design is the limited space available for an ohmic transformer, which is used to inductively drive the plasma current. Consequently spherical tori such as NSTX typically possess between 10 and 20% of the inductive volt-second capability of higher aspect ratio tokamaks with comparable minor radius, such as DIII-D[35]. This lower volt-second capability means that the achievement of long pulse discharges requires optimization of flux consumption, including the avoidance of large transient events such as Type I ELMs.

Large Type I ELMs in NSTX are often accompanied[34] by a rapid cold pulse that can propagate to the magnetic axis, reducing electron temperature and increasing plasma resistivity. To maintain constant plasma current, the loop voltage is transiently increased by the plasma control system, leading to more rapid ohmic flux consumption. An example is used to illustrate this point. A comparison of the flux consumption between a discharge with Type I ELMs and small Type V ELMs is shown in Figure 1. Panel (c) shows that the ohmic coil current ramp rate began to increase at the onset of large ELMs in panel (h) for #117425. Although #117425 ended prematurely due to the onset of a locked mode, a plasma current ($I_p$) flat-top out to t=0.8 sec is projected from the flux consumption rate prior to the locked mode. In contrast the discharge with small ELMs maintained an $I_p$ flat-top until t~0.97 sec, which was limited by ramp-down of the toroidal field and projected to last for another 100 msec if the toroidal field were extended, i.e. 33% longer than the discharge with large ELMs. In addition, #117424 maintained good energy confinement relative to the global ITER 97-L scaling law[36] (panel f). A small shape change was apparently responsible[37] for the difference in performance: starting from a balanced double-null, the upper X-point was pulled upward by about 4 cm in the discharge with small ELMs, such that the lower X-point became the dominant one. This movement corresponds to a 0.5cm difference of the two separatrices at the outer midplane, i.e. $\delta_r^{sep}$=-0.5 cm. This shape dependence is consistent with the characteristics observed[13] for Type V ELMs at lower $\delta \sim 0.4$, although the magnitude of

the increase of the upper X-point height required for small ELMs appears to be reduced at high $\delta$.

The example shown here is not unique: at least a half dozen small and large ELM comparison discharges have been obtained in NSTX, with similar results. Thus it is clear that the small ELMs are an important element in the achievement of a longer pulse length in NSTX. We now turn to discuss the structure of small ELMs from several diagnostics.

## III. Spatial and Temporal Structure of Type V ELMs

Interpretation of boundary phenomena is enabled by a set of diagnostics in NSTX that has been steadily growing since machine commissioning. The diagnostics discussed in this section include: 1) a fast framing wide-angle view visible camera; 2) a set of four ultra-soft X-ray (USXR) arrays; 3) several toroidally viewing interferometer chords; 4) an in-vessel toroidal Mirnov array; 5) a gas-puff imaging diagnostic; and 6) a fast framing visible camera with a tangential divertor view. Table I lists details of these diagnostics and the type of information provided by each on small ELM dynamics. Other boundary diagnostics not discussed in this paper but which provide additional small ELM data include: charge exchange recombination spectroscopy (CHERS) with sub-cm spatial resolution at the edge; a passive edge rotation diagnostic; several fast framing visible cameras with a choice of band-pass filters; several infrared cameras; several 1-D CCD cameras for filtered, visible light detection; a set of fast time response filterscopes; a fast reciprocating probe; and tile-imbedded Langmuir probes.

For the reader's convenience, we briefly summarize the basic picture of the Type V ELM from these diagnostics before going into the detailed discussion of each diagnostic signature. The Type V ELM appears as a single or sometimes double filamentary helical formation aligned with the magnetic field, first appearing on the closed field lines near the top of the H-mode pedestal, and propagating toroidally in the counter $I_p$ direction. The filaments drift radially outward as they move toroidally, eventually appearing on visible camera images of the entire plasma and the divertor region. A summary of the observations for each diagnostic is included at top of each sub-section below for ease of reading.

*III.1. Wide angle fast-framing visible camera signature*

The characteristic filamentary structure of a Type V ELM is perhaps best displayed with a midplane, fast-framing visible camera[38] using a wide-angle lens. A comparison of several different ELM types imaged with this camera was recently published[19]; here, we will expand on the helicity of the filament. The basic conclusion from the image is that the filament is well aligned with the total magnetic field at the edge.

Figure 2(a) shows an image of a Type V ELM filament captured with the fast camera in a lower-single null configuration (which nevertheless has a second X-point inside the vacuum vessel). The original image was unfiltered with a 10μs integration time, and time slice subtraction from a nearby frame was used for contrast enhancement to highlight the ELM perturbation. Note that the impact of the ELM on the lower divertor light was not determined because the lower divertor light was saturated in both the original and background time slices. Three different open field lines corresponding to normalized poloidal flux values ($\psi_N$) of 1.05, 1.20, and 1.49 are overlaid for comparison in panel (a). The first field line is between the first and second X-points, the second is outside the second X-point, and the third is far outside the second X-point and close to the radius of the limiter, i.e. the RF antenna.

This comparison suggests that the visible camera light originates mainly from the open field lines far outside of the second magnetic X-point, as no helical light structure is observed around the center stack as shown for the $\psi_N = 1.05$ field line, and the helicity of the field line at $\psi_N = 1.20$ does not quite match the image. Thus, it is apparent that a portion of the filament, which we will subsequently show to originate from the closed field lines, survives until it comes into contact with the nearest limiting surface at the midplane. The toroidal length of the filament from point A to point B in panel 2a is ~ 6m or about 2/3 of the toroidal circumference, largely independent of which field line is used for the estimate. For comparison, panel 2b shows a Type I ELM that was comprised of many independent filaments. We can state, albeit with limited statistics, that the small ELMs imaged with this camera are always composed of one or two filaments, i.e. far fewer than the number of filaments typically observed in large ELMs.

*III.2. Ultra-soft X-ray signature*

The USXR arrays in NSTX (Figure 3) measure line-integrated plasma emission with intensity $I \propto n_{e,edge}^2 T_{e,edge}^{0.5}$ when used in conjunction with Be filters of thickness between 3 and 10 μm[39]. Specifically, the 5 μm and 10 μm filters used for ELM studies reject emission below 400 and 600 eV respectively, corresponding to $T_e$ cutoffs of about 130 and 200 eV respectively for a Maxwellian distribution. In comparison, the NSTX H-mode pedestal $T_e$ ranges[19] from 100 to 300 eV, i.e. the USXR emission is indeed dominated by the pedestal plasma.

Variation of the filter thickness was used to localize the filament origin to the vicinity of the top of the H-mode pedestal in NSTX. To be specific, only a small fraction of the number of filaments observed with the 5 μm filter were observed with the 10 μm filter for identically programmed discharges, which suggests that nearly all of the filaments originated where the $T_e$ value was between 130 and 200 eV, i.e. the $T_e$ range at the top of the NSTX H-mode pedestal.

From the USXR data, a composite picture of the poloidal component of motion of the filaments comprising Type V ELMs can be ascertained. The filaments enter the field of view of the USXR arrays in the lower divertor region as indicated by the yellow circle in Figure 3, and propagate with an apparent poloidal component upward toward the outer midplane and then the top of the machine. As will be shown in subsequent sections, the filament is elongated along the field lines and its motion is more likely toroidal, yielding the observed apparent poloidal propagation observed in the USXR at this single toroidal location. For certain long-lived filaments, propagation on the high field side region down the center stack can be observed. We now illustrate the detailed motion of a single filament in each of the USXR arrays.

Data from a Type V ELM with the 5 μm filter on each array are shown in Figure 4. The bright bands indicate emission above the background. The signature and movement of the filament is indicated with the brown arrows in each panel. We begin our discussion with the bottom panel and move upward in the apparent direction of filament motion. The filament motion in panel 4d traces the shape of the letter "V" on the upward viewing array (black channels in Figure 3) starting at t ~ 0.3122 sec. The left side of the "V"

means that the radius of the chord on which the filament appeared was increasing, as shown schematically by the yellow arrow in Figure 3. The right side of the "V" means that the radius of the chord on which the filament appeared was decreasing. Thus, the filament propagated radially outward for ~ 0.2 msec, and then radially inward for another ~ 0.3 msec. Panel 4a shows a similar "V" shape for the downward-viewing array (green channels in Figure 3), except that the bottom tip of the "V" was cut off. The bottom of the "V" is truncated when the filament temporarily disappeared from the field-of-view near the outer midplane, because the chord coverage did not extend all the way to outer midplane (see Figure 3). Moreover, Panel 4a shows the left hand-side of a new "V" pattern (the right-most arrow) adjacent to the normal "V". This new "V" shape did not connect to the other "V" shape at the top of the panel because the filament moved around the top of the plasma, again outside the field of view of the downward-viewing array. Panels 4b and 4c show the filament propagated upward from the lower divertor region to the top of the machine (red and blue channels in Figure 3). Note the existence of a possible pre-cursor mode in panel 4c just before the filament movement; this mode was not always present prior to filament propagation in all Type V ELMs. We also note that while the filament lifetime was ~ 0.8-1 msec in Figure 4, it was typically 0.2-0.4 msec for most other Type V ELMs.

*III.3. Interferometer signature*

The plasma electron density along several different paths is measured with the far infrared tangential interferometry and polarimetry (FIReTIP) system[40]. Figure 5 shows a plan view of the NSTX, along with the line-of-sight of four interferometer chords and the toroidal location of several other diagnostics and hardware. Note in particular that the intersection of chord #3 and the edge plasma occurs very close to the USXR diagnostic port, allowing verification that the same filament is being imaged by these two diagnostics. The excess density in the filaments above the background plasma density, and the toroidal rotation of the filaments are clearly observed on the FIReTIP chords. Given the rotation speed, an estimate of the filament toroidal length can be obtained. Finally the filament size perpendicular to the magnetic field along a flux surface can be

estimated by assuming the filament is aligned with the total magnetic field, as shown by the visible camera image in Figure 2.

We now summarize the observations from the interferometer analysis: 1) the filaments rotate counter to the plasma current with speeds between 5 and 15 km/sec; 2) the half-width of the filaments normal to the total field along the same flux surface ranges between 6 and 18 cm; and 3) about 60% of the Type V ELMs are comprised of single filaments, whereas the rest are mostly comprised of two separate filaments. The supporting data for each of these points is discussed below.

The filament shown in Figure 4 is clearly observed as a density perturbation on the interferometers in Figure 6. Panels 6a and 6b show the filament on a lower divertor channel and a midplane channel of the midplane-mounted downward viewing USXR array of panel 4c. Note that an excess density perturbation was observed propagating from FIReTIP channel 1 -> 2 -> 3 from t=0.31234 to 0.3125 sec; the timing of the disturbance on channel 3 occurred just after the peak in panel 6b, confirming that the same filament was observed. A strong perturbation was not observed on chord #4 in panel 6f, indicating that the filament had a finite radial extent and had not at that time drifted out to the chord #4 tangency radius of R=1.50m. Based on the known spacing between the interferometer chords at the plasma edge at R ~ 1.4 m, the toroidal rotation speed of the filament was between -5 and -7 km/sec. Here we use the negative sign for the rotation speed because the filament rotation was in the direction opposite the plasma current, and opposite to the neutral beam momentum input direction. For reference, the measured fully stripped carbon rotation velocity near the top of the H-mode pedestal was typically ~ 10-20 km/sec from the CHERS diagnostic in similar discharges, including the one with multiple filaments in Figure 7 (see discussion below). Another perturbation is seen propagating from channel 3 -> 2 -> 1 from 0.31286 – 0.31288 sec in Figure 6, apparently close to the interferometer port. From the known spacing between chords at the plasma edge, the toroidal rotation velocity is computed between -8 and -10 km/sec, and it is probable that the same filament caused both perturbations.

An estimate of the filament toroidal extent at the outer midplane can be obtained from the product of the width of the perturbation across each interferometer chord and the rotation speed between chords computed above; note that the four cm finite spot size of

the FIReTIP beam must be taken into account. Note that this toroidal extent is not the full length of ~ 5-6m shown in Figure 2, but rather a measure of the size of the perturbation normal to the total magnetic field along a flux surface at the outer midplane. Assuming that the filament follows field lines, the relation between the toroidal extent and the size normal to the field is given by the local magnetic field pitch. Using this technique the toroidal extent at the midplane ($L_\phi$) is estimated at between 18 cm and 30 cm for the filament in Figure 6. The filament width perpendicular to the magnetic field along a flux surface ($L_\perp$) is then between 10 cm and 16 cm, obtained by multiplying the toroidal length by the sine of the field line pitch angle ~ $35^o$. Finally the vertical extent of the filament at the midplane ($L_Z$) is estimated between 13 and 20 cm, obtained by multiplying the toroidal length by the tangent of the field line pitch angle. The size and speed characteristics of the filament in Figure 6 are summarized in Table II. An examination of several Type V ELMs yields a range of toroidal propagation speeds between -5 and -15 km/sec, and a range of perpendicular widths between 6 and 18 cm. Statistical averages of toroidal speed and lengths from ~ one dozen filaments is displayed in Table III. Thus the filaments are elongated toroidally and poloidally relative to a plausible radial dimension of several cm, and can be thought of more as a ribbon or sheet than a cylinder, bent into a helical shape. Note that a modest acceleration of the filaments as they approach the FIReTIP port, e.g. from –6km/sec to –10 km/sec as displayed for a single filament in Table II, is commonly observed.

Multiple filaments are sometimes observed simultaneously during Type V ELMs. An example of the signatures of multiple filaments is shown in the FIReTIP data in Figure 7. A perturbation propagating from channels 3 -> 2 -> 1 was observed at t=0.2593 sec (dashed arrow), followed by another one at t=0.2595 sec (dotted arrow). A third perturbation propagating from channels 1 -> 2 -> 3 was observed at t=0.2598 sec (dashed arrow). The FIReTIP perturbations are correlated with in a single peak in the outer and inner divertor $D_\alpha$ emission in panels (f) and (g) respectively. Based on the toroidal rotation speed computed as discussed above, it is likely that the same filament was responsible for the first perturbation and the third perturbation on the FIReTIP data, and that a second filament was responsible for the second peak. In contrast to the first perturbation, the second filament showed a clear signature on channel #4, indicating it

was near or outside of R=1.50 the tangency radius of that FIReTIP channel. At this time, the separatrix from EFIT reconstructions[41, 42] was computed at R ~ 1.46m, i.e. the second filament was in the scrape-off layer. These filaments did not have the characteristic signature in USXR emission with the Be10 μm filter as shown in Figure 4, indicating that the origin of the filaments occurred somewhere in radius where the $T_e < 200$ eV.

A survey of about 50 Type V ELMs indicated that about 60% of the ELMs had a single filamentary perturbation on the FIRETIP data, whereas about 40% had two filamentary perturbations during the divertor $D_\alpha$ rise time. Because of the finite toroidal coverage of the FIReTIp channels, a toroidal mode number as high as n=3 or n=4 would be consistent with these multiple filament observations if the filaments were evenly distributed toroidally. This assessment of the number of separate perturbations was based on the toroidal rotation speed. If the toroidal speed between channels 1-3 far away from the FIReTIP port was within a factor of two of the speed between channels 1-3 close to the port, then it was assumed that a single filament could have caused the FIReTIP perturbations, otherwise at least two filaments would have been necessary. In contrast, a survey of several large Type I ELMs showed at least four separate filamentary perturbations on the FIReTIP data during the $D_\alpha$ rise time, consistent with a toroidal mode number $12<n<16$.

*III.4. Magnetics signature*

NSTX is equipped with a toroidal Mirnov array that can detect the electromagnetic signature of Type V ELMs, as well as the toroidal propagation speed and direction. In addition, the excess current carried in the filament can be estimated from the absolutely calibrated magnetic field perturbation at the wall.

We have previously shown an n=1 pre-cursor[43] to the Type V ELM crash on the fast magnetics data; in fact, that pre-cursor is simply the electromagnetic signature of the filament at the wall sensor. The magnetic signature and propagation of the filament from the discharge in Figure 4 is shown in Figure 8. The toroidal propagation speed obtained from the contour plot is ~ 6-10 km/sec, i.e. similar to the values reported from the FIReTIP analysis in Table II. The maximum vertical field perturbation of this filament was ~ 2 G, indicating that the filament carried between 300 and 500 A of current, with

the precise value depending on the actual radial location of the current centroid. This current flows in the same direction as the plasma current and in the opposite direction of the filament motion.

*III.5 Outer Midplane Gas Puff Imaging signatures*

The poloidal and radial structure of the small ELMS just above the outer midplane was investigated with the gas puff imaging (GPI) diagnostic[38, 44]. The GPI diagnostic consists of a fast-framing, filtered visible camera viewing a neutral gas cloud from a manifold along the direction of the edge magnetic field. This results in a 2-D image of the light pattern in the radial-poloidal plane. Neutral transport calculations have shown that the visible light observed by GPI straddles the separatrix at the outer midplane[45]. We note that the GPI diagnostic has been primarily used to characterize short-lived ($\tau_{auto} \leq 0.05$ msec) electrostatic turbulence-driven filaments, which appear to be distinct from the electromagnetic filaments during Type V ELMs in several ways.

The vertical and radial size and motion of the filaments can be measured with GPI. Generally, we observe poloidally-elongated structures with size ~ 10-15 cm (full-width half-max), with radial correlation lengths of a few cm. These structures differ from the normal electrostatic filaments which have comparable poloidal and radial correlation lengths[44]. When combined with the above diagnostic observations, a picture of the Type V ELM filament emerges as a ribbon-like structure, with radial propagation speed less than 1 km/sec.

An example of a small ELM imaged with the GPI diagnostic in $D_\alpha$ light is shown in Figure 9, albeit from a different discharge than for the diagnostics shown above. A poloidally-extended coherent light pattern is observed in frame #149, and this structure moves first radially outward in frame#150-151, and then poloidally upward in frames #152-154. Frames #155-158 show the relaxation to the normal H-mode light emission profile. The upward motion is consistent with the motion inferred from the USXR images in Figure 4. The poloidal length of the coherent structure is up to ~ 15 cm in the GPI data, i.e. well within the range of vertical lengths observed for other Type V ELMs as inferred from the interferometer data in Table III. The radial width of the light pattern associated with the ELM is about 3 cm, confirming the picture of the filament as a

poloidally/toroidally extended, and radially localized ribbon-like formation. The radial propagation speed estimated from frames #149-153 is ~ 600 m/sec.

Assuming that the 3 cm radial width of the structure in the GPI images is indicative of the radial width of the filament ($\lambda_{fil}$), the excess density in the filament $\delta n_e^{fil}$ can be estimated as $\delta n_e^{fil}/\overline{n_e} \sim \delta n_e^{FIR}/\overline{n_e} \times \lambda_{FIR}/\lambda_{fil}$, where $\delta n_e^{FIR}$ is the size of the perturbation on the FIR channels and $\lambda_{FIR}$ is path length of the FIReTIP beam through the plasma. Using the density perturbations from the most perpendicular FIReTIp chord, e.g. chord #1 in Figures 6 and 7, the density perturbation $\delta n_e^{FIR} \sim$ 1.4-2% and plasma path length $\lambda_{FIR} \sim$ 3m, an excess density in the filament $\delta n_e^{FIR}/\overline{n_e}$ ~140-200% is estimated.

*III.6. Scrape-off Layer and Divertor Visible Camera signatures*

When the Type V ELM filaments drift radially outward across the separatrix, they interact with the scrape-off layer (SOL) plasma, emptying the power and particles into the divertor and wall. After crossing into the SOL, parallel flow along the open magnetic field lines to the targets competes with radial propagation across the magnetic field. Part of the ELM pulse is thought to flow at the ion sound speed to the outer target, and the remainder flows the longer way around the magnetic field lines to the inner target. This flow to each target is imaged effectively with a new fast-framing video camera[46] with a tangential view of the lower divertor, shown in Figure 10. In particular, the poloidal propagation speed of individual filaments, along with the number of filaments within a given ELM, can be ascertained.

Figure 11 shows a set of frames during a Type V ELM in C-II light: the first signature in panel (b) is a bright band radially outboard of the outer strike point (appears as fuzz in the frame), followed by a single filamentary type perturbation propagating down the inner SOL in panels (c) and (d). We interpret the increase in light intensity as a combination of the effects of enhanced density and enhanced temperature in the filament on the carbon atomic physics; separation of the density and temperature dependencies is beyond the scope of this paper and will be pursued in future analysis. The X-point light pattern is affected in panel (e), but the ELM does not appear to fully connect to the inner target. Based on correlation analysis of the filamentary perturbation down the inner SOL, the poloidal propagation speed of Type V ELMs is between 0.5 and 2.0 km/sec,

depending on the particular ELM. A deceleration of the poloidal speed is evident as the perturbation approaches the X-point where the poloidal field vanishes. In comparison, Figure 12 shows the SOL perturbation during a Type III (or possibly a low amplitude Type I) ELM. The first signature is a bright zone near the outer strike point in panel (b), followed by a reconnection of the detached inner divertor leg in panel (c) near the separatrix. Panel (d) shows a complex structure comprised on many filaments moving poloidally down the inner SOL leg toward the X-point. In summary, the two main differences we wish to highlight are: 1) single vs. multiple filaments for Type V and III ELMs respectively, and 2) reconnection of the plasma to the inner target during a Type III ELM, but not a Type V ELM.

## IV. Theory Implications and Preliminary Stability Calculations

We now consider the lifetime of Type V ELMs in the context of the widely accepted picture of ELMs as peeling-ballooning modes. Once the edge plasma crosses the stability boundary, theory predicts that the ballooning mode grows explosively, coalescing into one or more filaments which are ejected radially from the plasma. Indeed filament and finger-like protrusions are observed in simulations of the non-linear MHD phase of the ballooning instability[28, 29, 47]. In this picture, the filaments can expand radially until they strike a material surface at the midplane, similar to the image shown in Figure 2a and first reported[17] in MAST. A characteristic filament detonation time has been derived[47] as $\tau_{det} \sim (\tau_A^2 \tau_E)^{1/3}$, where $\tau_A$ and $\tau_E$ are the Alfven time and the energy confinement time respectively. For conditions typical of the NSTX pedestal just before a Type V ELM, $\tau_{det} \sim 0.12$ msec, which is considerably shorter than the Type V ELM filament life time of 0.4-1 msec. Hence it may be concluded that the single filament of the Type V ELM is not in the non-linear detonation phase. This conclusion has certain ramifications. In recent peeling-ballooning calculations, ELMs are correlated with intermediate-n (n=toroidal mode number) instabilities[26, 27, 30], which can sometimes coalesce into single filamentary structures during the non-linear evolution phase of ~ 0.1 msec[31]. The implication is that the instability responsible for the radially localized Type V ELMs *originates* as a low-n instability because it persists for 10 times the expected non-linear growth time scale. However low-n instabilities are normally associated with perturbations of large radial

extent, expected to cause a sizeable drop in stored energy, which is inconsistent with the Type V ELM characteristic of having an immeasurably small impact on stored energy.

Preliminary edge stability calculations were done for NSTX with the ELITE[26, 27] and DCON[48] codes, using a model equilibrium and the measured pedestal $n_e$ and $T_e$ at the onset of Type V ELMS (t=0.245s) for the discharge in Figure 7. The relevant shape and discharge parameters are given in Table IV. The edge current density was assumed to be due entirely to the bootstrap current, as calculated with the Sauter model[49]. For these input conditions, intermediate to high-n ballooning modes were found to be robustly stable. However, low to intermediate-n kink/peeling modes may be either stable or unstable depending upon the details of the assumed current profile near the separatrix. Although the underlying mechanism for Type V ELMs has not yet been clearly identified, the current-driven kink/peeling modes are a candidate for further analysis. Additional edge current density constraints on the equilibrium and several new edge Thomson channels presently being commissioned will help refine the parameters in Table IV and enable more detailed stability calculations.

## V. Summary, Discussion and Conclusions

We have presented evidence that small, Type V ELMs are an important ingredient of the longest pulse discharges in NSTX, and we have described the formation and evolution of the small ELMs. The small Type V ELM is composed of a small number of helical filaments: typically one or two are observed but three or four are possible due to limited spatial coverage of the diagnostics. The first sign pf the ELM appears either in the ultra-soft X-rays near the top of the H-mode pedestal, or as an excess density perturbation propagating toroidally in adjacent interferometer channels. Rotation speeds of ~ 10 km/sec and perpendicular correlation lengths of ~ 10 cm are estimated from the interferometer data. The filaments drift radially outward as they rotate toroidally in the direction opposite the plasma current and the background plasma rotation. During the outward radial drift into the visible light region, the filaments are observed by the gas-puff imaging diagnostic as a poloidally extended but radially localized structure, confirming the picture of a ribbon-like formation. When the filaments are captured on a

wide-angle camera, a clear helical structure is observed, aligned with the total magnetic field. This structure can persist into the far SOL.

Thus, a composite picture of the structure and drift of the filaments obtained from the multiple diagnostics discussed above has been obtained. The toroidal component of this motion is represented in cartoon form with field line tracing and variation of the toroidal viewing angle in Figure 13, to simulate filament motion in the direction opposite to $I_p$ and the NBI input direction. It is apparent from this cartoon that a diagnostic viewing in a single poloidal plane would first observe the perturbation in the lower divertor, followed by an apparent upward motion, which is precisely the pictures obtained from soft X-ray data, e.g. in Figure 4.

After connecting with the open field lines in the SOL, Type V ELMs are observed to behave like other ELM types, i.e. the particle flux reaches the outer divertor first, followed by a perturbation down the inner SOL. Even in the inner SOL, the Type V ELMs still have only a single or double filament structure, and the ELM particle flux does not appear to reach all the way to the inner target. Note that mechanism of interaction between the ELM flux and the SOL plasma, whether through a magnetic reconnection or through degeneracy[50] of the flux surfaces near the X-point, cannot be determined from the data presented here.

Identification of the underlying instability responsible for the Type V ELM has been unsuccessful to date. The Type V ELM filaments persist for time scales much longer than the characteristic filament detonation time scales predicted by ballooning theory, which are typically ~ 100 μsec or less. Preliminary calculations indicate that the edge plasma pressure gradient is below the ideal MHD peeling-ballooning limit, but the firmness of this conclusion with regard to the current driven modes may well be limited by diagnostic spatial resolution, as well as limited knowledge of the edge current profile. Recent diagnostic upgrades will improve the input for these stability calculations, and a more concerted effort to obtain optimized data from all diagnostics simultaneously for the same set of discharges is planned.

## VI. Acknowledgements

This research was supported by the U. S. Dept. of Energy under contracts DE-AC05-00OR22725, DE-AC02-76CH03073, DE-FC02-04ER54698, W-7405-ENG-48 and grants DE-FG02-99ER54524, DE-FG02-04ER54767, DE-FG03-99ER54518, DE-FG03-99ER54519, DE-FG03-99ER51069, and DE-FG02-99ER54523. The filterscope data shown in Figure 7 were enabled through a diagnostic collaboration between NSTX and DIII-D. We gratefully acknowledge the contribution of the NSTX technical staff and neutral beam operations staff.

**Figure Captions**

1. (Color Online) Illustration of the effect of ELM size on pulse length: (a) plasma current ($I_p$), (b) neutral beam injected power ($P_{NBI}$), (c) current in the ohmic transformer ($I_{OH}$), (d) line-average density from interferometry ($\bar{n}_e$), (e) plasma stored energy from equilibrium reconstructions ($W_{MHD}$), (f) confinement time relative to the ITER 97-L global scaling law, (g) lower divertor $D_\alpha$ emission for small ELM discharge, and (h) lower divertor $D_\alpha$ emission for large ELM discharge. The solid (black) discharge has only small, Type V ELMs, whereas the dashed (blue) discharge contains large, Type I ELMs.

2. (Color) Visible camera pictures in unfiltered light of a single-filament Type V ELM with a wide-angle midplane view in panel (a), as compared with a higher toroidal mode number perturbation from a Type I ELM in panel (b). The image in (a) is from #113024, using the frame at 0.52 sec after subtracting a background frame from t=0.515 sec. The NSTX center stack hardware and a set of edge field lines at the $\psi_N$ = 1.05, 1.20, and 1.49 surfaces are overlaid in panel (a); the distortion caused by the wide-angle lens was simulated in overlaying the hardware and field line traces onto the camera image. Panel (b) is from #112581, using the frame at 0.500 sec after subtracting a background frame from t=0.495 sec.

3. (Color) View chords of the ultra-soft X-ray (USXR) arrays in NSTX. The yellow circle shows the typical poloidal location where the filamentary perturbations associated with Type V ELMs entered the field-of-view of the USXR arrays. All arrays are in the same (R,Z) plane. The filaments usually propagated poloidally upward away from the lower X-point, as indicated by the yellow arrows.

4. (Color) Signature of Type V ELM on USXR arrays, using a 5 μm Be filter: (a) top-mounted, downward viewing array, (b) midplane-mounted, upward viewing array, (c) midplane-mounted downward viewing array, and (d) bottom-mounted upward viewing array. The colors in the caption correspond to the colored arrays shown in Figure 3. Data were acquired at 190 kHz have contrast enhanced to emphasize the filament movement.

5. (Color) Plan view of NSTX, showing location of Far-Infrared Tangential Interferometer chords. The toroidal location of the USXR arrays and filterscopes for $D_\alpha$ measurements are also indicated.

6. (Color Online) Toroidal propagation of Type V ELM observed in interferometer channels. (a) USXR channel viewing lower divertor (hup_02), (b) USXR channel viewing midplane (hup_15), (c) FIReTIP channel #1, (d) FIReTIP channel #2, (e) FIReTIP channel #3, (f) FIReTIP channel #4, and (g) lower divertor B-II line emission. Time delay of the filamentary perturbation between interferometer chords is used to estimate the ELM toroidal rotation speed, and the duration along a single chord indicates toroidal size.

7. (Color Online) Toroidal propagation of Type V ELM observed in interferometer channels with multiple simultaneous filaments. (a) FIReTIP channel #1, (b) FIReTIP channel #2, (c) FIReTIP channel #3, (d) FIReTIP channel #4, and (e) lower, outboard divertor $D_\alpha$ line emission at R=0.79 m, and (f) lower, inboard divertor $D_\alpha$ line emission at R=0.33 m.

8. (Color Online) Contour plot of data from the high-n toroidal magnetics array during the Type V ELM from #113665 shown in Figure 4. The toroidal angle shown on the y-axis increases in the counter-clockwise, co-$I_p$ direction shown in the plan view in Figure 5. The toroidal motion of the filament in the counter $I_p$ direction is highlighted by the yellow arrows.

9. (Color) Edge $D_\alpha$ light obtained with the gas-puff imaging diagnostic for a Type V ELM from #113410. Each frame has a 10 μs exposure, and the first frame starts at 0.45147 sec. The separatrix (as computed by equilibrium reconstruction) is indicated by the dashed line, and the shadow of the radio frequency antenna is indicated by the solid line in each frame.

10. (Color) Schematic representation of the NSTX lower divertor area and field-of view of the fast framing divertor visible camera. The outer strike point shown in Figures 11 and 12 is indicated here by the bright yellow band.

11. (Color) Frame sequence showing signature of Type V ELM in the SOL and divertor with the fast framing camera in C-II light (filter center=657.8 nm, full-width half-max=1.5 nm, 5 μs exposure, 10 μs between adjoining frames). A single filamentary perturbation is observed. The X-point geometry is overlaid in panel (a) for guidance, and the center stack is outside the field-of view on the left hand side.

12. (Color) Frame sequence of Type III ELM in the SOL and divertor with the fast framing camera in C-II light (filter center=657.8 nm, full-width half-max=1.5 nm, 5 μs exposure, 10 μs between adjoining frames). Multiple filamentary perturbations are observed to move down the inner SOL leg. The X-point geometry is overlaid in panel (a) for guidance, and the center stack is outside the field-of view on the left hand side.

13. (Color) Field line traces used to simulate the toroidal propagation of a Type V ELM filament, based on #113024 at t=0.52 sec. A field line in the SOL with $\psi_N = 1.12$ is viewed from several toroidal angles, simulating motion of a helical structure elongated along the magnetic field lines and propagating counter to the NBI input. The toroidal viewing angles are indicated.

Table I. Diagnostic information relevant to small ELM structure and evolution.

| Diagnostic | Quantity Measured | Location | Specific information |
|---|---|---|---|
| Main plasma fast visible camera | Unfiltered visible light | Wide angle view inside most of the vacuum vessel | Snapshot of filament toroidal and poloidal extent |
| Ultra-soft X-ray arrays | USXR emission with filter dependent $T_e^{min}$ | Single poloidal plane, with plasma emission mainly from the edge (Figure 3) | • Duration<br>• $T_e$ at radial origin of instability<br>• Poloidal propagation speed and direction |
| Interferometers | Line integrated electron density $\overline{n_e}$ | Four toroidal chords (Figure 5) | • Number of filaments<br>• Toroidal propagation speed and direction<br>• Excess electron density in filaments $\delta n_e^{filament}$<br>• Filament size $L_\perp$ |
| In-vessel magnetics | Perturbed magnetic field at the wall $\delta B_z^{wall}$ | Toroidal Mirnov array | • Toroidal mode number n<br>• Duration<br>• Toroidal propagation speed and direction<br>• Excess current in filaments $\delta I_z^{ELM}$ |
| Gas Puff Imaging | Visible light filtered for $D_\alpha$ | Outer midplane at one toroidal location, with plasma emission near the separatrix | • Radial/vertical size<br>• Radial/vertical propagation speed and direction |
| Divertor fast visible camera | Visible light filtered for C-II | Lower X-point and SOL region | • Number of filaments in SOL<br>• Poloidal propagation speed and direction in the SOL |

Table II. Characteristic size (half-width) and velocity of a single Type V ELM filament observed in the FIReTIP channels for the filament shown in Figure 6, from discharge #113665. Toroidal rotation velocity ($v_\phi$) was computed between the FIReTIP channel in question and the nearest one in the counter clockwise direction shown in Figure 5. The toroidal ($L_\phi$), perpendicular along a flux surface ($L_\perp$) and vertical lengths ($L_Z$) are estimated as the filament passes through the outer midplane. * The characteristics of the filament observed in the signals from channel 1 (far(near)) were computed using the channel 2 (far(near)) rotation speeds. Hear "near" and "far" refer to whether the filament is passing through the edge plasma close to the FIReTIP port or nearly $180^0$ away (see Figure 5).

| Channel Number | Peak Time (msec) | Width (msec) | $v_\phi$ (km/sec) | $L_\phi$ (cm) | $L_\perp$ (cm) | $L_Z$ (cm) |
|---|---|---|---|---|---|---|
| 1 (far)* | 312.346 | 0.039 | --- | 0.18 | 0.10 | 0.12 |
| 2 (far) | 312.425 | 0.039 | -5.5 | 0.18 | 0.10 | 0.12 |
| 3 (far) | 312.508 | 0.037 | -6.3 | 0.20 | 0.11 | 0.14 |
| 3 (near) | 312.861 | 0.039 | -7.3 | 0.25 | 0.14 | 0.17 |
| 2 (near) | 312.874 | 0.032 | -9.8 | 0.28 | 0.16 | 0.20 |
| 1 (near)* | 312.874 | 0.028 | --- | 0.25 | 0.14 | 0.15 |

Table III. Average size (half-width) and velocity and fractional standard deviations from a dozen long-lived Type V ELM filaments observed in the FIReTIP channels from discharges #113665 and #117405-117419. Toroidal rotation velocity ($v_\phi$) was computed between the FIReTIP channel in question and the nearest one in the counter clockwise direction shown in Figure 5. The negative sign was removed from the values and indicated in the column heading for clarity. The range in values results from assuming the filament is centered radially either at R=1.4m or at R=1.5m, i.e. about 5cm either inside or outside of the separatrix. Note the speeds and sizes decrease for channel 2 (near) because the path length decreases in going from R=1.4 to 1.5m close to the FIReTIP port. The toroidal ($L_\phi$), perpendicular along a flux surface ($L_\perp$) and vertical lengths ($L_Z$) are estimated as the filament passes through the outer midplane.

| Channel Number | $-v_\phi$ k□□□□ σ | $L_\phi$ □) σ | $L_\perp$ □) σ | $L_Z$ □) σ |
|---|---|---|---|---|
| 2 (far) | 7.6-7.8 (±16%) | 0.13-0.14 (±45%) | 0.08-0.08 (±45%) | 0.09-0.10 (±45%) |
| 3 (far) | 6.4-6.4 (±16%) | 0.12-0.12 (±51%) | 0.07-0.07 (±51%) | 0.08-0.09 (±51%) |
| 3 (near) | 8.8-10.0 (±15%) | 0.16-0.18 (±31%) | 0.09-0.10 (±31%) | 0.11-0.13 (±31%) |
| 2 (near) | 11.6-10.2 (±24%) | 0.19-0.15 (±34%) | 0.11-0.09 (±34%) | 0.13-0.11 (±34%) |

Table IV. Discharge characteristics used in preliminary stability calculations – from #117414 at t=0.245s.

| *Quantity* | *Value* |
|---|---|
| Plasma Current | 0.8 MA |
| Toroidal Field on axis | 0.45 T |
| Major radius | 0.85 m |
| Minor radius | 0.62m |
| Elongation | 2.0 |
| Lower triangularity | 0.45 |
| Upper triangularity | 0.35 |
| Magnetic balance ($\Delta_r^{sep}$) | -2.5 cm |
| Edge $Z_{eff}$ | 2.3 |
| Central $Z_{eff}$ | 1.2 |
| Central, pedestal $n_e$ | 2.7e19, 4.0e19 |
| Central, pedestal $T_e$ | 0.75 keV, 0.12 keV |
| Central, pedestal $T_i$ | 1.0 keV, 0.12 keV |
| Pedestal $n_e$ width | 5% |
| Pedestal $T_e$ width | 3% |
| Pedestal $T_i$ width | Same as $T_e$ width |
| □□□□□□□□ β | 8% |
| $\beta_N$ | 2.6 |
| Internal inductance | 0.7 |
| Safety factor on axis, minimum | 2.0, 2.0 |
| Edge safety factor, q95 | 7.8 |

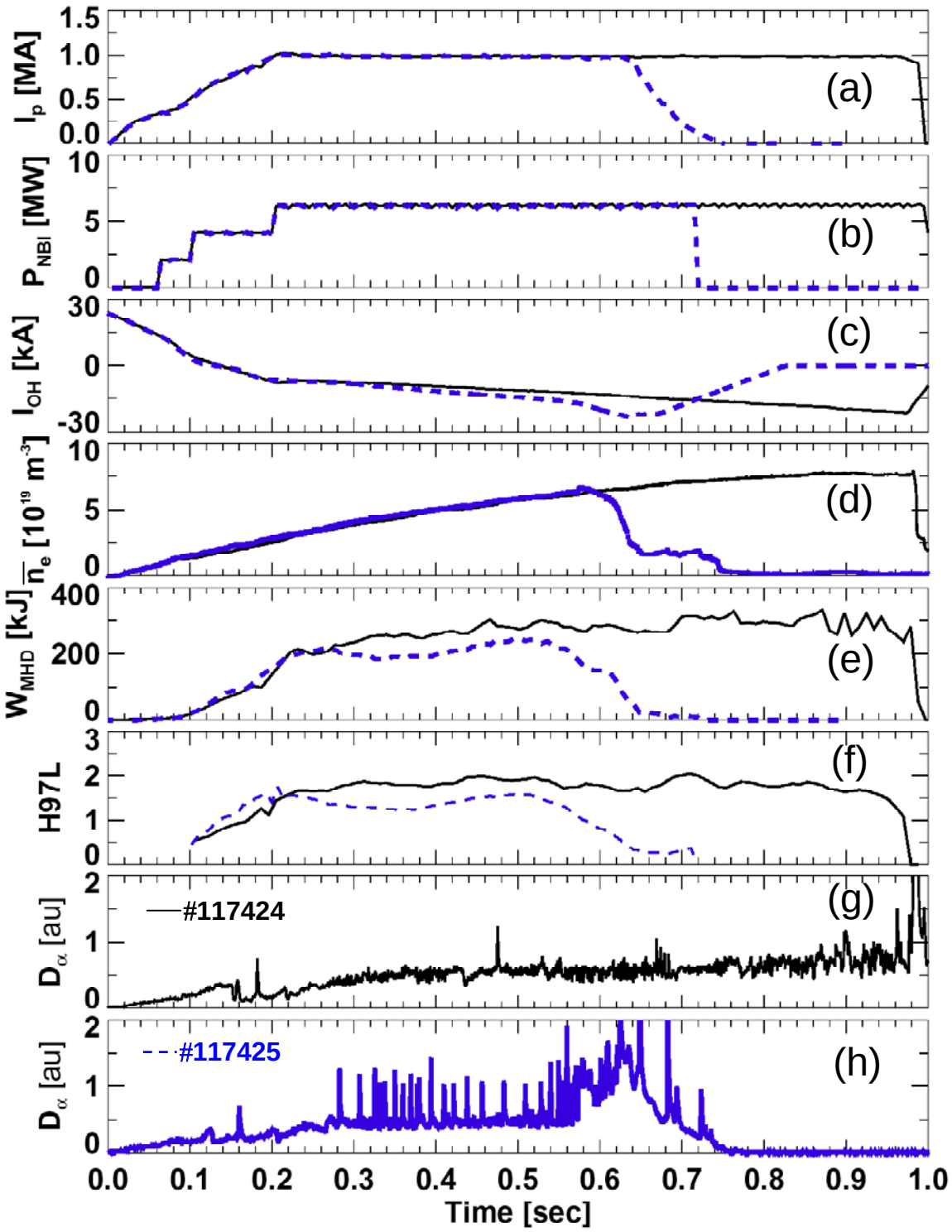
$I_p$ [MA]
$P_{NBI}$ [MW]
$I_{OH}$ [kA]
$\overline{n}_e$ [$10^{19}$ $m^{-3}$]
$W_{MHD}$ [kJ]
H97L
$D_\alpha$ [au]
$D_\alpha$ [au]
(a)
(b)
(c)
(d)
(e)
(f)
(g)
(h)
#117424
#117425
Time [sec]

Figure 1

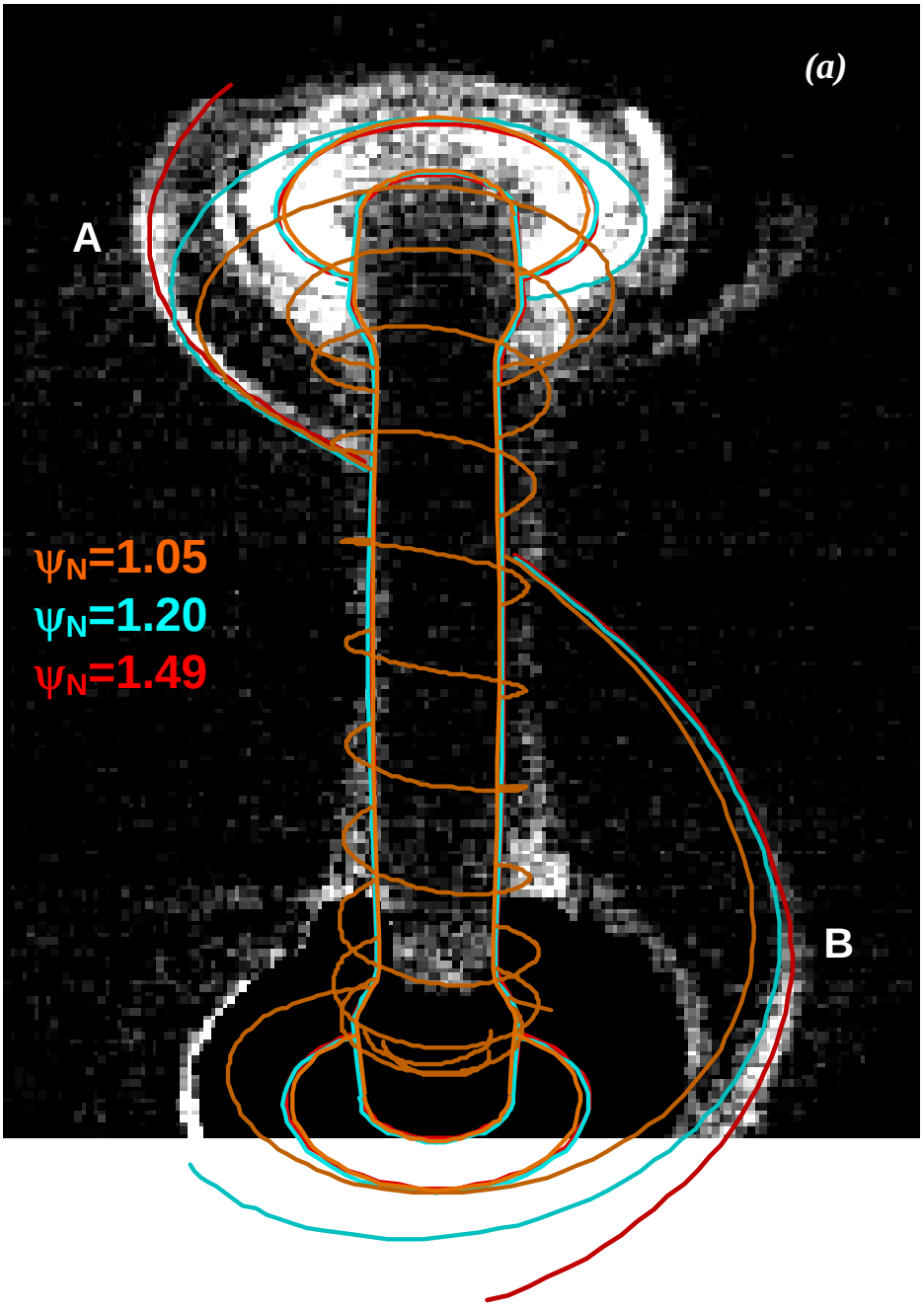


Figure 2a

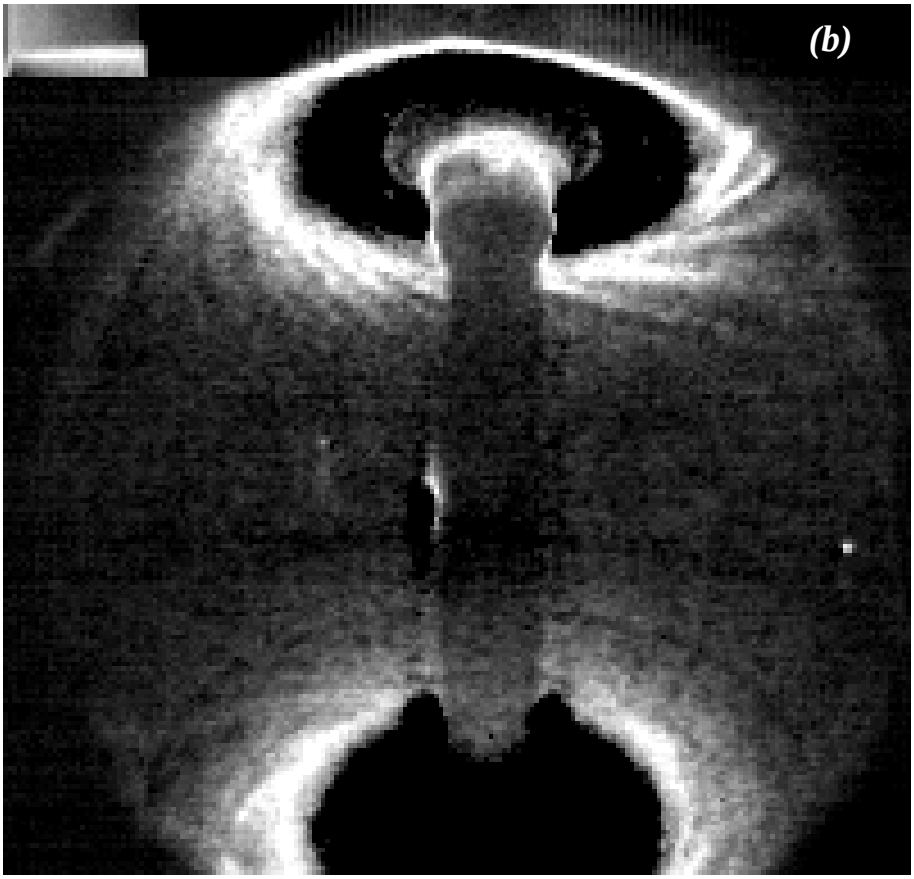


Figure 2b

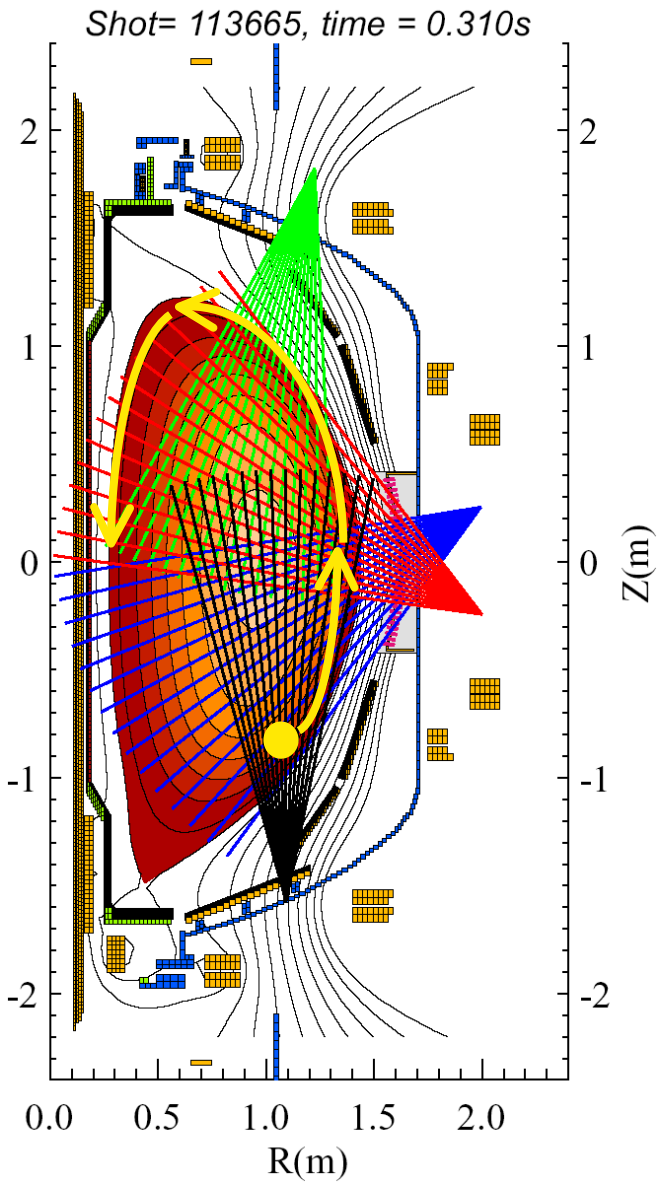


Figure 3

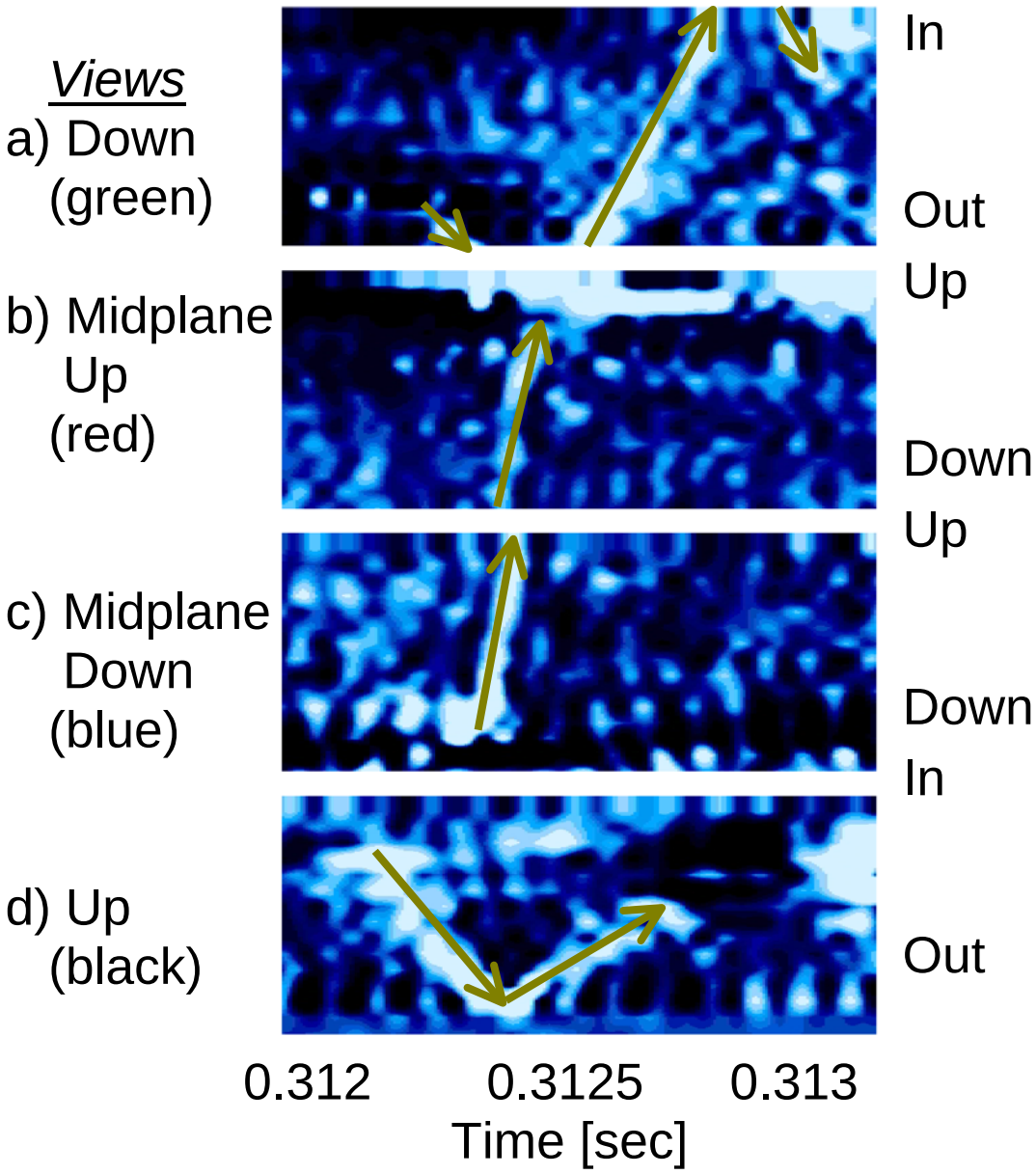
Views
a) Down
(green)
b) Midplane
Up
(red)
c) Midplane
Down
(blue)
d) Up
(black)
In
Out
Up
Down
Up
Down
In
Out
0.312
0.3125
0.313
Time [sec]

Figure 4

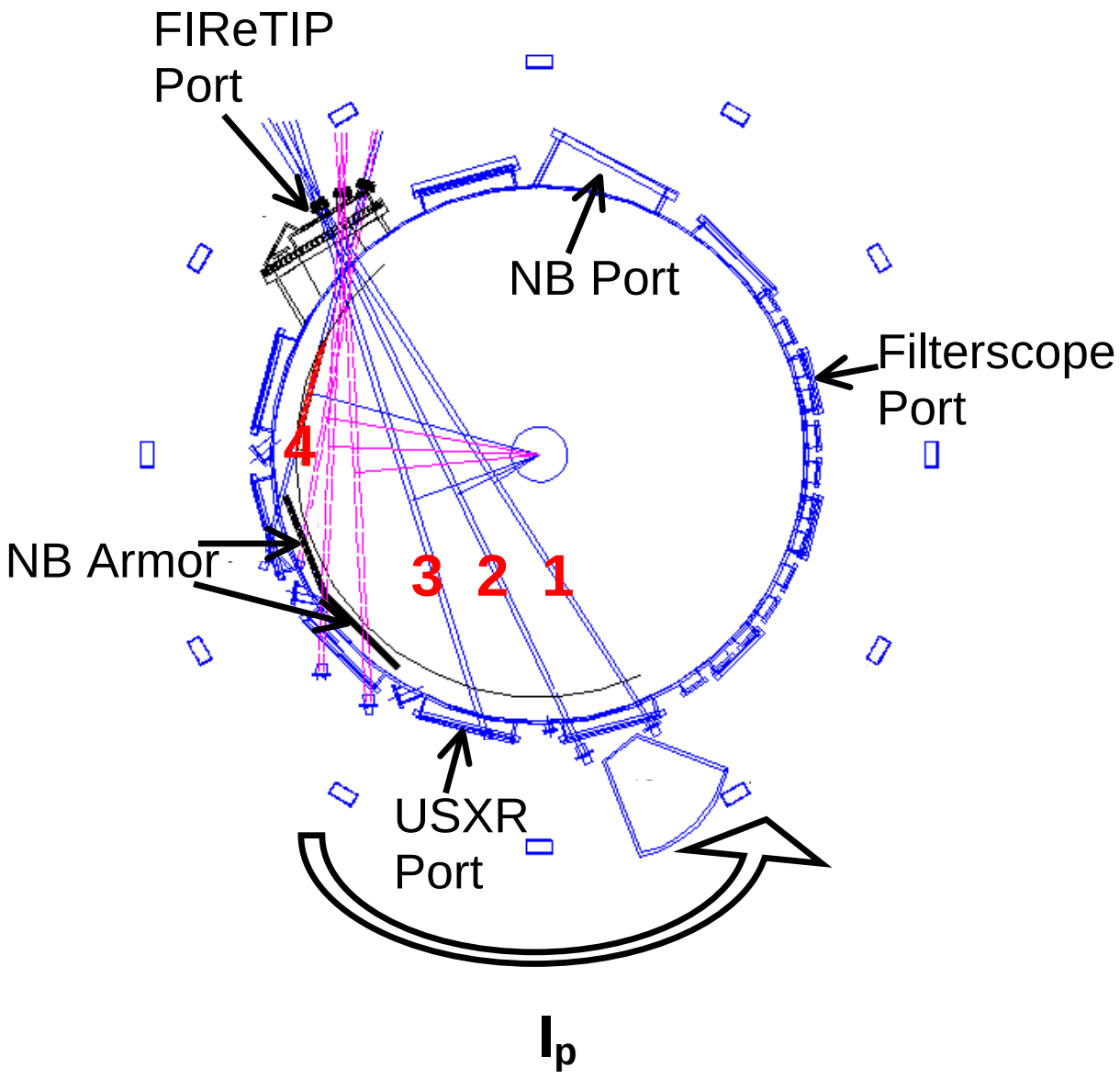
FIReTIP
Port
NB Port
Filterscope
Port
4
NB Armor
3
2
1
USXR
Port
$I_p$

Figure 5

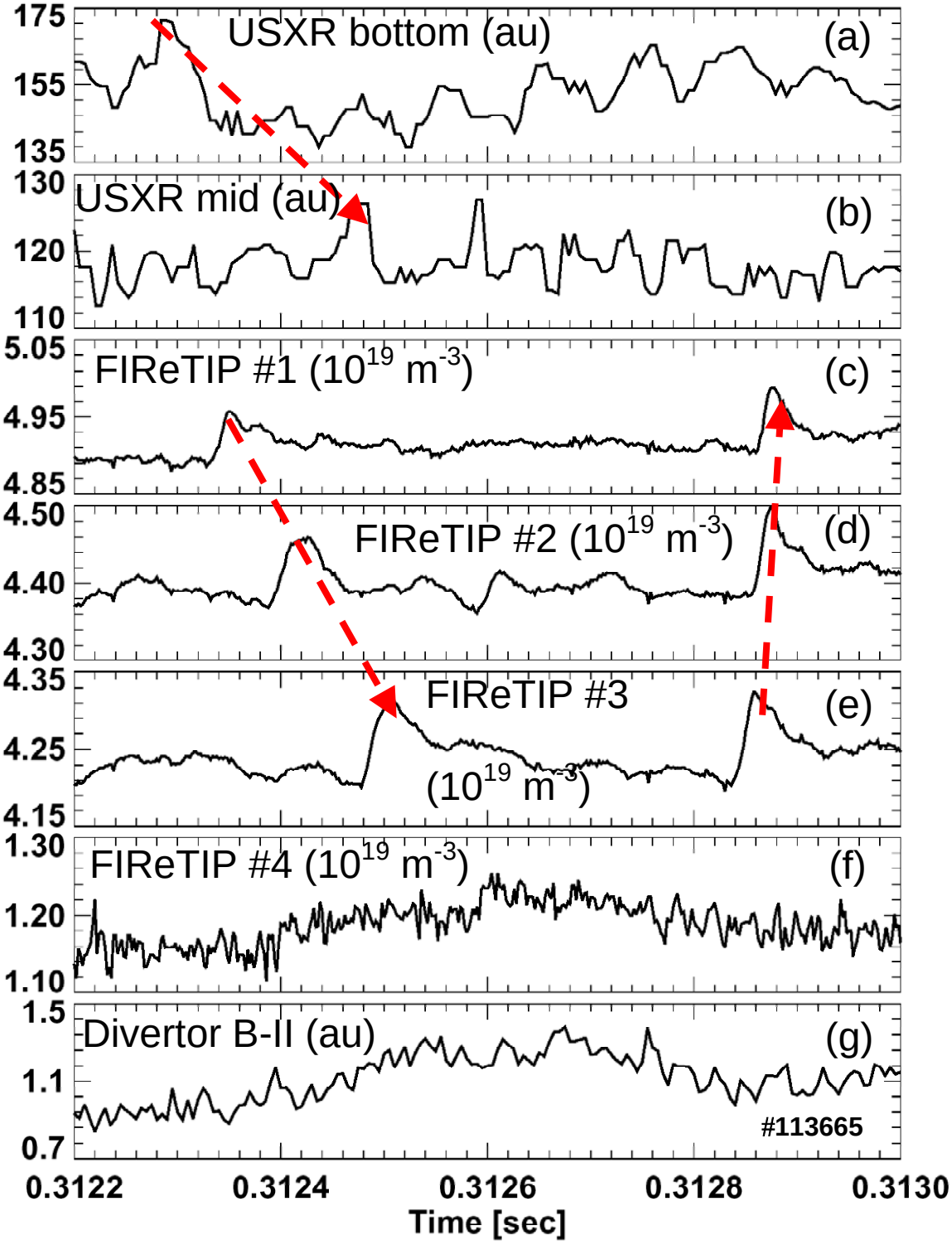
USXR bottom (au)
(a)
USXR mid (au)
(b)
FIReTIP #1 ($10^{19}$ $m^{-3}$)
(c)
FIReTIP #2 ($10^{19}$ $m^{-3}$)
(d)
FIReTIP #3
($10^{19}$ $m^{-3}$)
(e)
FIReTIP #4 ($10^{19}$ $m^{-3}$)
(f)
Divertor B-II (au)
(g)
#113665
175
155
135
130
120
110
5.05
4.95
4.85
4.50
4.40
4.30
4.35
4.25
4.15
1.30
1.20
1.10
1.5
1.1
0.7
0.3122
0.3124
0.3126
0.3128
0.3130
Time [sec]

Figure 6

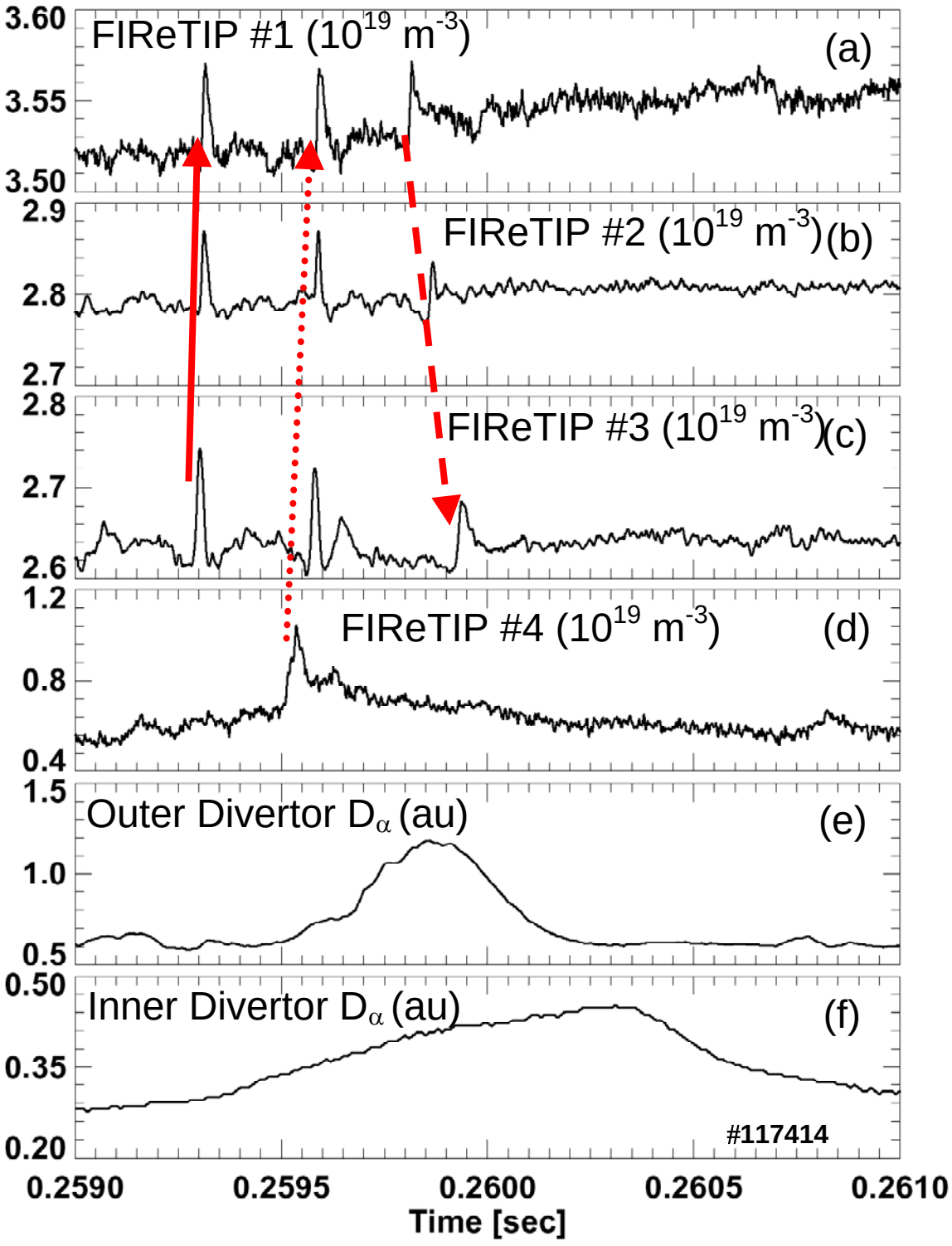
FIReTIP #1 ($10^{19}$ $m^{-3}$)
(a)
FIReTIP #2 ($10^{19}$ $m^{-3}$)
(b)
FIReTIP #3 ($10^{19}$ $m^{-3}$)
(c)
FIReTIP #4 ($10^{19}$ $m^{-3}$)
(d)
Outer Divertor $D_\alpha$ (au)
(e)
Inner Divertor $D_\alpha$ (au)
(f)
#117414
3.60
3.55
3.50
2.9
2.8
2.7
2.8
2.7
2.6
1.2
0.8
0.4
1.5
1.0
0.5
0.50
0.35
0.20
0.2590
0.2595
0.2600
0.2605
0.2610
Time [sec]

Figure 7

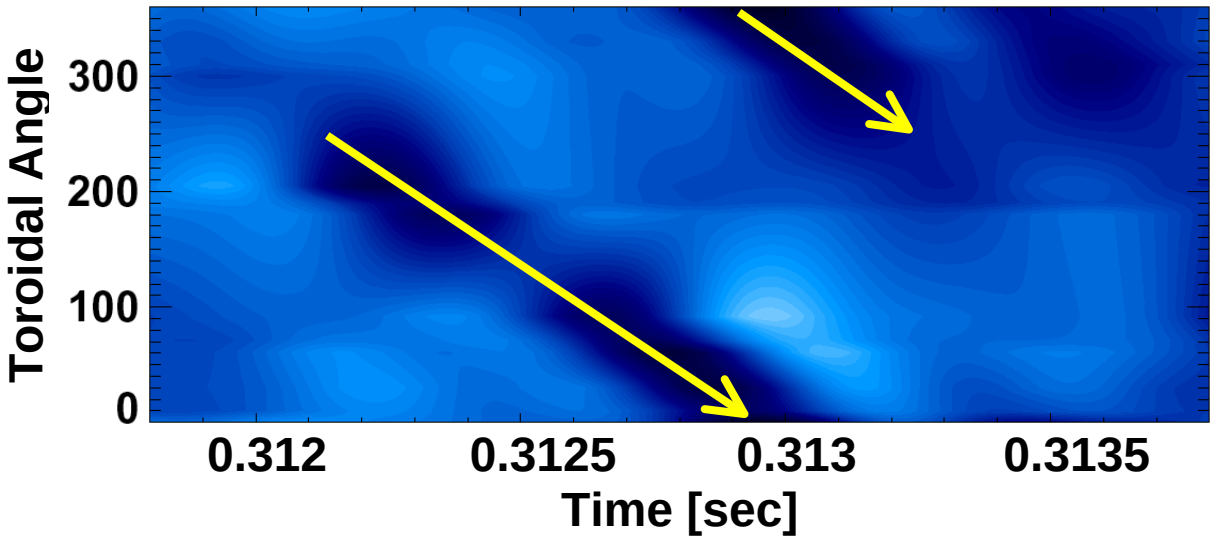


Figure 8

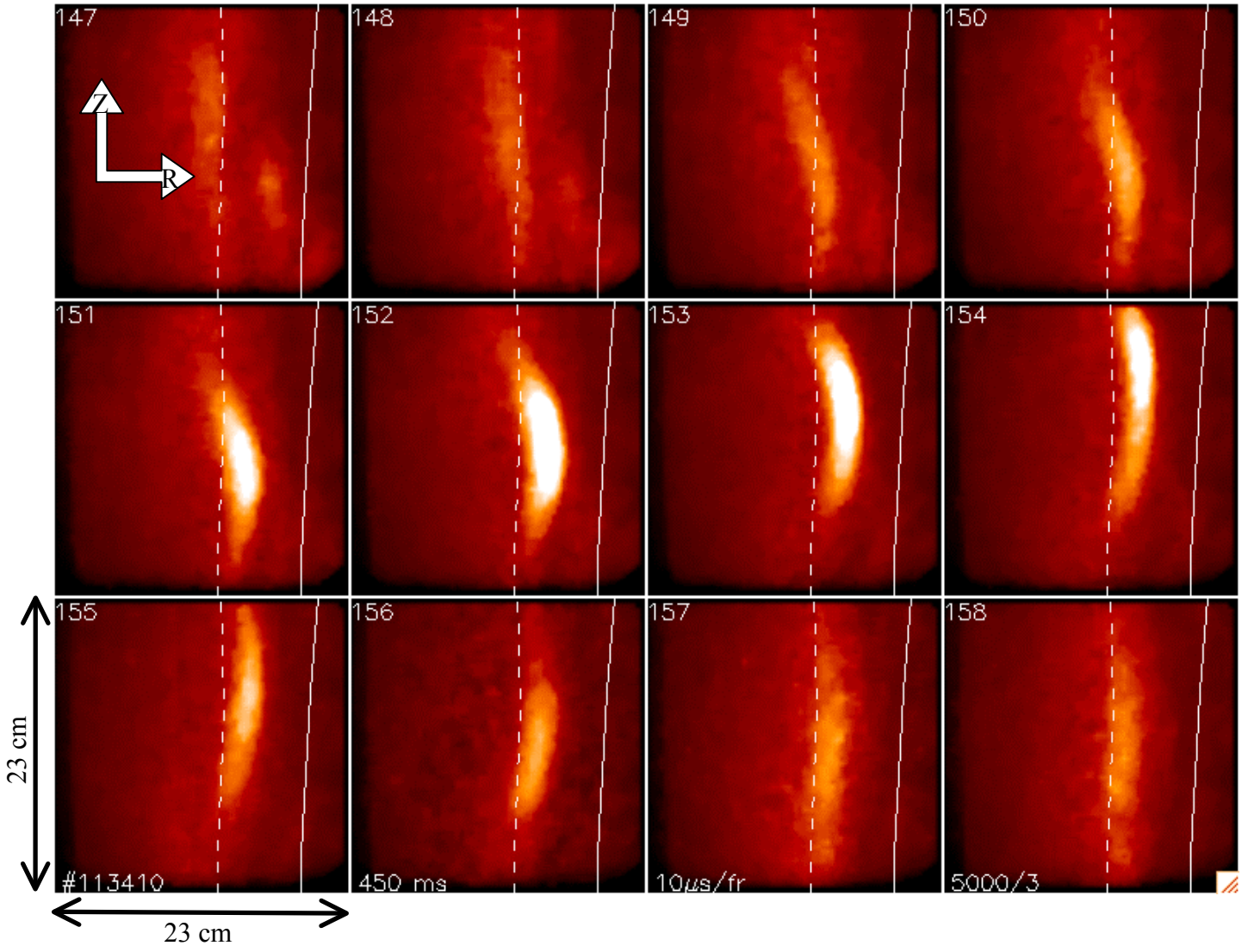
147
148
149
150
151
152
153
154
155
156
157
158
Z
R
#113410
450 ms
10μs/fr
5000/3
23 cm
23 cm

Figure 9

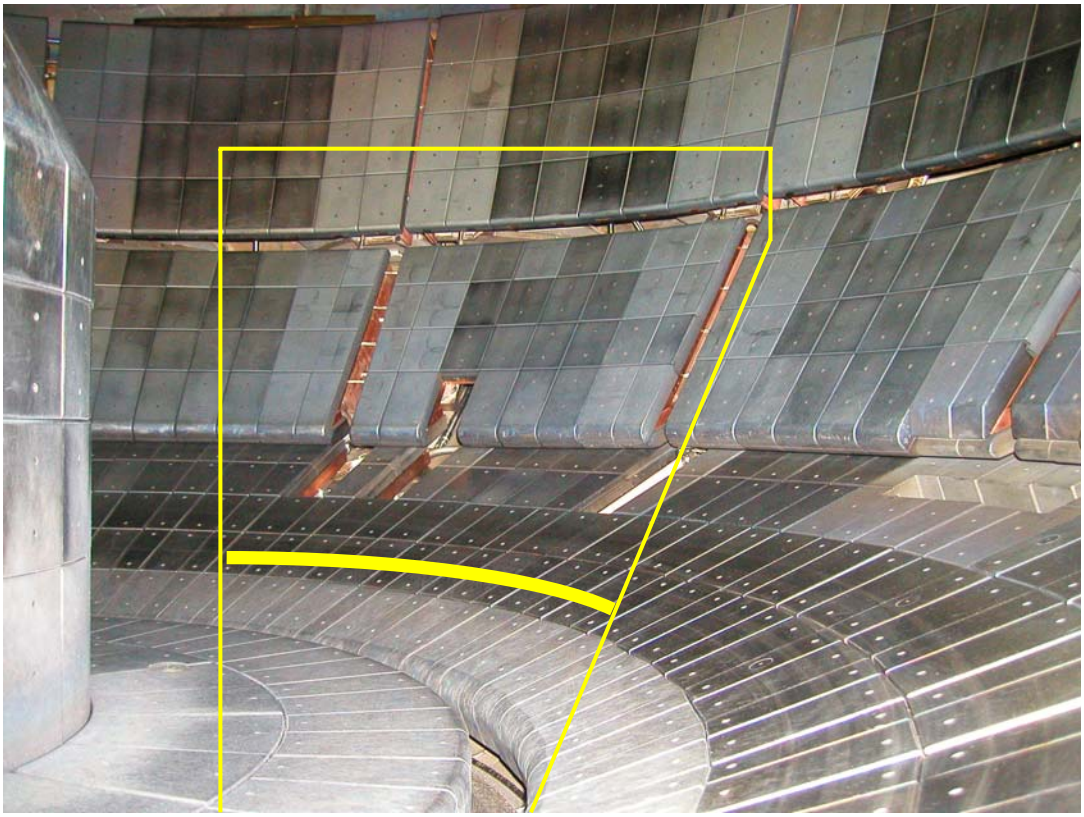

Figure 10

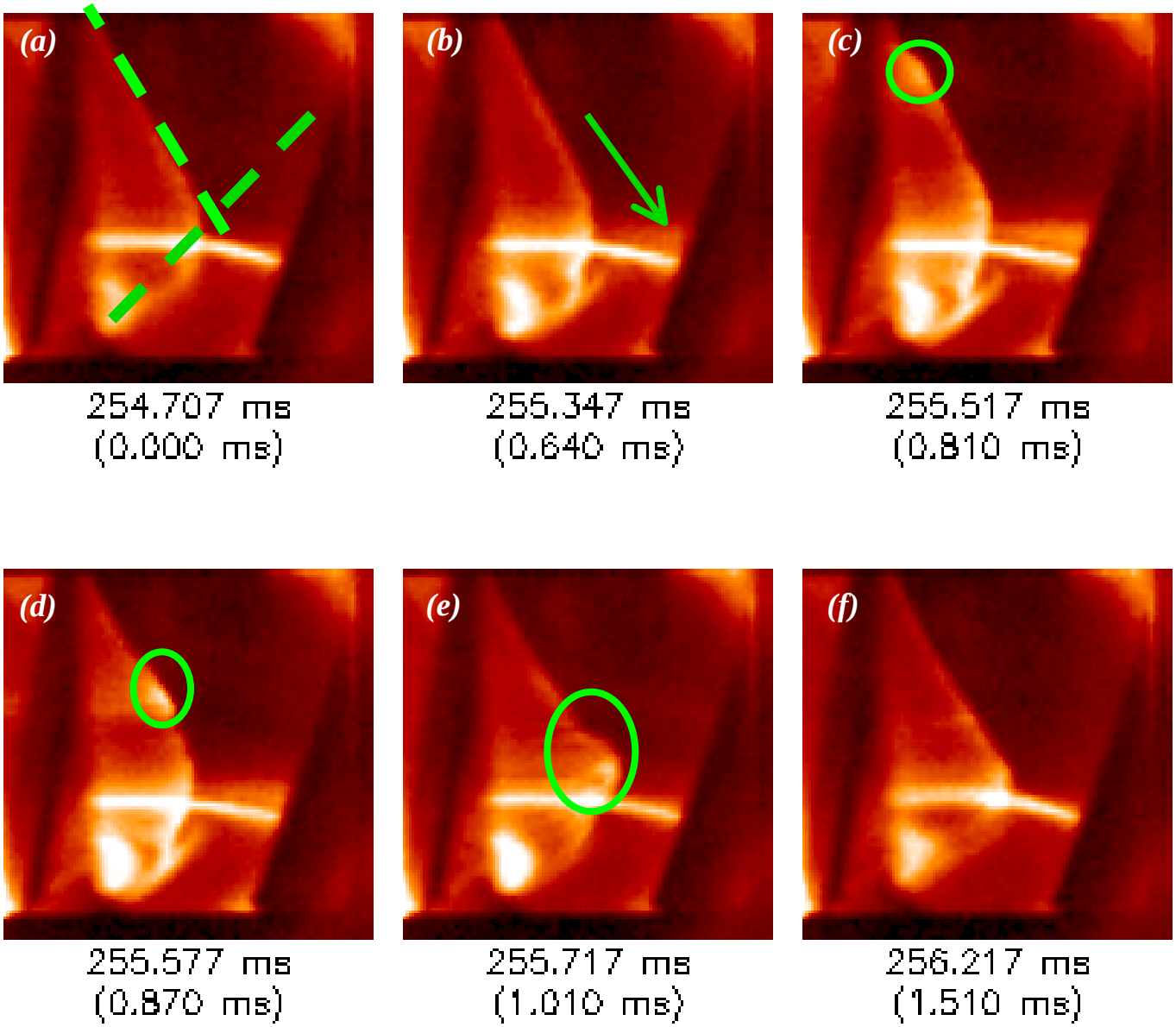
(a)
(b)
(c)
254.707 ms
(0.000 ms)
255.347 ms
(0.640 ms)
255.517 ms
(0.810 ms)
(d)
(e)
(f)
255.577 ms
(0.870 ms)
255.717 ms
(1.010 ms)
256.217 ms
(1.510 ms)

Figure 11

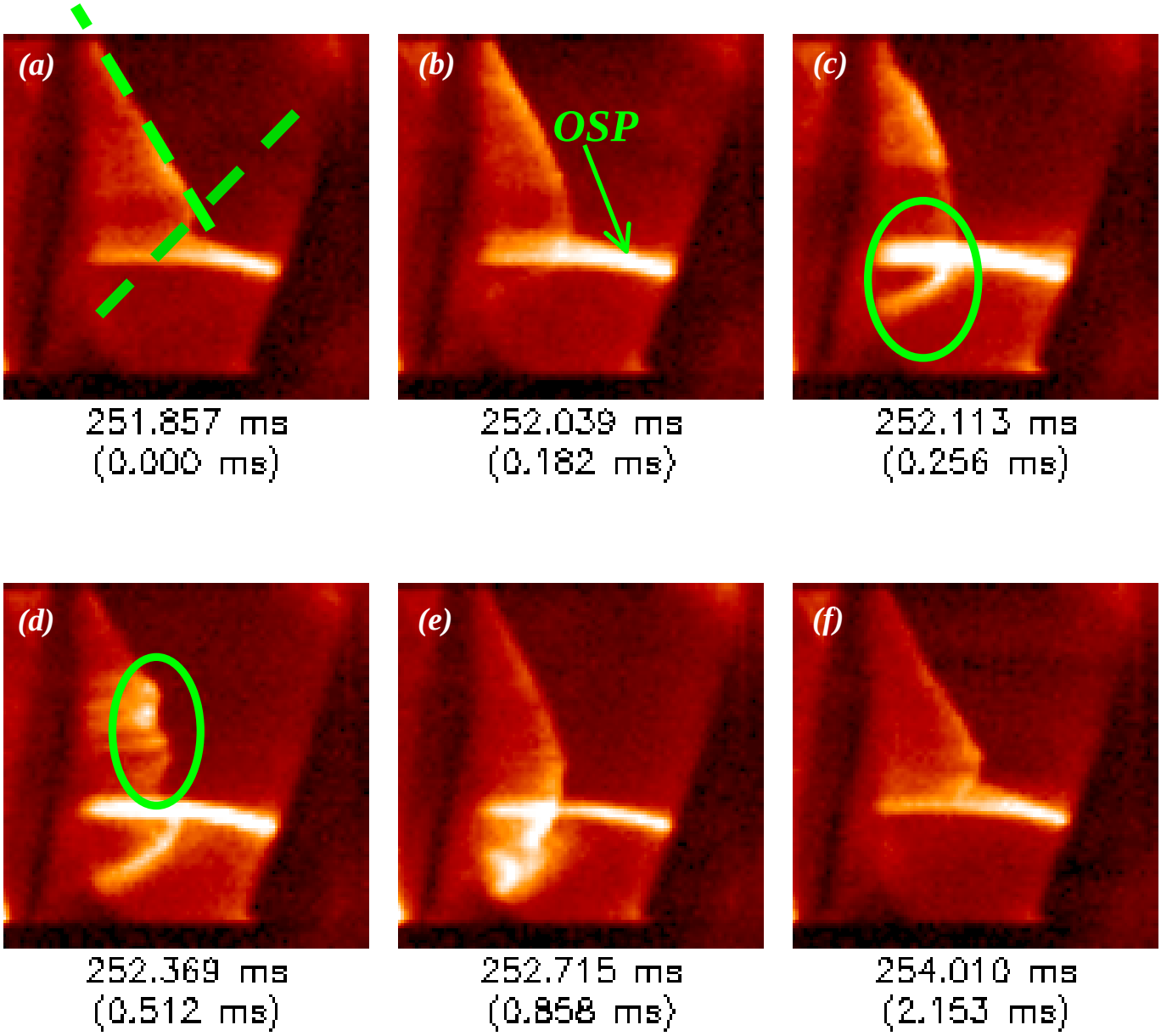
(a)
(b)
OSP
(c)
251.857 ms
(0.000 ms)
252.039 ms
(0.182 ms)
252.113 ms
(0.256 ms)
(d)
(e)
(f)
252.369 ms
(0.512 ms)
252.715 ms
(0.858 ms)
254.010 ms
(2.153 ms)

Figure 12

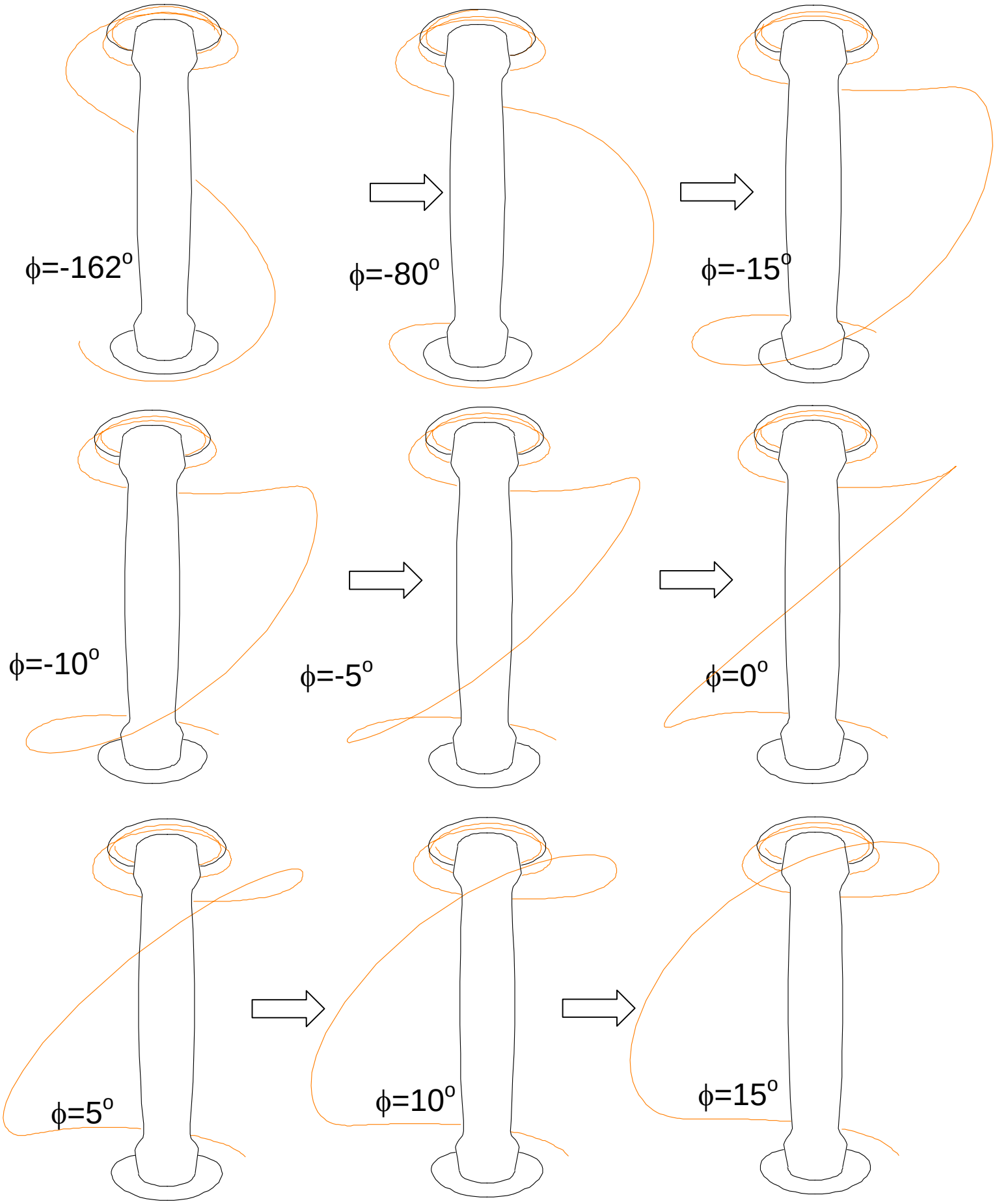


Figure 13

## References


[1] A. W. Leonard, A. Herrmann, K. Itami, et. al., Journal of Nuclear Materials **266-269**, 109 (1999).

[2] A. Loarte, G. Saibene, R. Sartori, et. al., Plasma Physics Controlled Fusion **45**, 1549 (2003).

[3] G. Federici, P. Andrew, P. Barabaschi, et. al., J. Nucl. Materials **313-316**, 11 (2003).

[4] T. Ozeki, M.S. Chu, L.L. Lao, T.S. Taylor, M.S. Chance, S. Kinoshita, K.H. Burrell, and R.D. Stambaugh, et. al., Nuclear Fusion **30**, 1425 (1990).

[5] J. Stober, M. Maraschek, G.D. Conway, et. al., Nuclear Fusion **41**, 1123 (2001).

[6] G. Saibene, P.J. Lomas, R. Sartori, et. al., Nuclear Fusion **45**, 297 (2005).

[7] A. W. Leonard, T.H. Osborne, M.E. Fenstermacher, and M.A. Mahdavi, et. al., Journal of Nuclear Materials **290-293**, 1097 (2001).

[8] G. Saibene, R. Sartori, A. Loarte, et. al., Plasma Physics Controlled Fusion **44**, 1769 (2002).

[9] Y. Kamada, T. Oikawa, L.. Lao, T. Takizuka, T. Hatae, A. Isayama, J. Manickam, M. Okabayashi, T. Fukuda, and K. Tsuchiya, et. al., Plasma Physics Controlled Fusion **42**, A247 (2000).

[10] Y. Takase, R. L. Boivin, F. Bombarda, et. al., Physics of Plasmas **4**, 1647 (1997).

[11] K. Kamiya, H. Kimura, H. Ogawa, H. Kawashima, K. Tsuzuki, M. Sato, Y. Miura and JFT-2M Group, et. al., Nuclear Fusion **43**, 1214 (2003).

[12] C. M. Greenfield, K.H. Burrell, J.C. DeBoo, et. al., Physical Review Letters **86**, 4544 (2001).

[13] R. Maingi, K. Tritz, E. Fredrickson, et. al., Nuclear Fusion **45**, 264 (2005).

[14] T. E. Evans, R.A. Moyer, P.R. Thomas, et. al., Physical Review Letters **92**, article #235003 (2004).

[15] P. Ghendrih, Y. Sarazin, M. Becoulet, et. al., J. Nucl. Materials **313-316**, 914 (2003).

[16] T. Eich, A. Herrmann, J. Neuhauser, and ASDEX Upgrade Team, et. al., Physical Review Letters **91**, 195003 (2003).

[17] A. Kirk, H.R. Wilson, G.F. Counsell, et. al., Physical Review Letters **92**, 245002 (2004).

[18] J. A. Boedo, D.L. Rudakov, E. Hollmann, et. al., J. Nucl. Materials **337-339**, 771 (2005).

[19] R. Maingi, C.E. Bush, E.D. Fredrickson, et. al., Nuclear Fusion **45**, 1066 (2005).

[20] M. Groth, M.E. Fenstermacher, J.A. Boedo, N.H. Brooks, D.S. Gray, C.J. Lasnier, A.W. Leonard, G.D. Porter, and J.G. Watkins, et. al., J. Nucl. Materials **313-316**, 1071 (2003).

[21] H. Takahashi, E.D. Fredrickson, M.J. Schaffer, M.E. Austin, T.E. Evans, L.L. Lao and J.G. Watkins, et. al., Nuclear Fusion **44**, 1075 (2004).

[22] A. Kirk, T. Eich, A. Herrmann, et. al., Plasma Physics Controlled Fusion **47**, 993 (2005).

[23] N. Nishino, L. Roquemore, T.M. Biewer, S.J. Zweben, R. Maqueda, R. Maingi, C. Bush, K. Tritz, D. Stutman, and NSTX team, et. al., IEEJ Trans. FM **125**, 902 (2005).

[24] J. W. Connor, R.J. Hastie, and J.B. Taylor, et. al., Physical Review Letters **40**, 396 (1978).
[25] J. W. Connor, R.J. Hastie, H.R. Wilson, and R.L. Miller, et. al., Physics of Plasmas **5**, 2687 (1998).
[26] H. R. Wilson, P.B. Snyder, G.T.A. Huysmans, and R.L. Miller, et. al., Physics of Plasmas **9**, 1277 (2002).
[27] P. B. Snyder, H. R. Wilson, J. R. Ferron, L. L. Lao, A. W. Leonard, T. H. Osborne, A. D. Turnbull, D. Mossessian, M. Murakami, and X. Q. Xu, et. al., Physics of Plasmas **9**, 2037 (2002).
[28] S. C. Cowley, H.R. Wilson, O. Hurricane, and B. Fong, et. al., Plasma Physics Controlled Fusion **45**, A31 (2003).
[29] H. R. Wilson, and S.C. Cowley, et. al., Physical Review Letters **92**, #175006 (2004).
[30] P. B. Snyder, H R Wilson, T H Osborne, and A W Leonard, et. al., Plasma Physics Controlled Fusion **46**, A131 (2004).
[31] P. B. Snyder, H.R. Wilson, and X.Q. Xu, et. al., Physics of Plasmas **12**, 056115 (2005).
[32] M. Ono, S.M. Kaye, Y.-K.M. Peng, et. al., Nuclear Fusion **40**, 557 (2000).
[33] S. M. Kaye, M.G. Bell, R.E. Bell, et. al., Nuclear Fusion **45**, S168 (2005).
[34] C. E. Bush, M.G. Bell, R.E. Bell, et. al., Physics of Plasmas **10**, 1755 (2003).
[35] J. L. Luxon, and L.G. Davis, et. al., Fusion Technology **8**, 441 (1985).
[36] S. M. Kaye, M. Greenwald, U. Stroth, et. al., Nuclear Fusion **37**, 1303 (1997).
[37] D. A. Gates, et. al., Physics of Plasmas, submitted (2005).
[38] R. J. Maqueda, G.A. Wurden, S. Zweben, L. Roquemore, H. Kugel, D. Johnson, S. Kaye, S. Sabbagh, and R. Maingi, et. al., Review of Scientific Instruments **72**, 931 (2001).
[39] D. Stutman, M. Finkenthal, H. W. Moos, K. B. Fournier, R. Kaita, D. Johnson, and L. Roquemore, et. al., Review of Scientific Instruments **74**, 1982 (2003).
[40] K. C. Lee, C. W. Domier, M. Johnson, N. C. Luhmann, Jr., and H. Park, et. al., Review of Scientific Instruments **75**, 3433 (2004).
[41] L. L. Lao, H. St. John, R.D. Stambaugh, A.G. Kellman, and W. Pfeiffer, et. al., Nuclear Fusion **25**, 1611 (1985).
[42] S. A. Sabbagh, S.M. Kaye, J. Menard, et. al., Nuclear Fusion **41**, 1601 (2001).
[43] R. Maingi, S.A. Sabbagh, C.E. Bush, et. al., J. Nucl. Materials **337-339**, 727 (2005).
[44] S. J. Zweben, R.J. Maqueda, D.P. Stotler, et. al., Nuclear Fusion **44**, 134 (2004).
[45] D. P. Stotler, D. A. D'Ippolito, B. LeBlanc, R. J. Maqueda, J. R. Myra, S.A. Sabbagh, and a. S. J. Zweben, et. al., Contribution to Plasma Physics **44**, 294 (2004).
[46] R. J. Maqueda, R. Maingi, K. Tritz, K. C. Lee, C. E. Bush, E. D. Fredrickson, J. E. and A. L. R. Menard, S. A. Sabbagh, S. J. Zweben, et. al., J. Nucl. Materials, submitted 5/2006 (2006).
[47] S. C. Cowley, and M. Artun, et. al., Physics Reports **283**, 185 (1997).
[48] A. H. Glasser, et. al., Bull. Am. Phys. Soc. **42**, 1848 (1997).
[49] O. Sauter, C. Angioni, and Y.R. Lin-Liu, et. al., Physics of Plasmas **6**, 2834 (1999).

[50] T. E. Evans, R. K. W. Roeder, J. A. Carter, B. I. Rapoport, M. E. Fenstermacher, and C. J. Lasnier, et. al., J. Physics: Conf. Series **7**, 174 (2005).

The Princeton Plasma Physics Laboratory is operated
by Princeton University under contract
with the U.S. Department of Energy.

Information Services
Princeton Plasma Physics Laboratory
P.O. Box 451
Princeton, NJ 08543

Phone: 609-243-2750
Fax: 609-243-2751
e-mail: pppl_info@pppl.gov
Internet Address: http://www.pppl.gov